Heterojunction of nanostructured α-Fe_2O_3/CuO for enhancement of photoelectrochemical water splitting

Pannan I. Kyesmen[1], Nolwazi Nombona[2] and Mmantsae Diale[1]
[1]*Department of Physics, University of Pretoria, Private Bag X20, Hatfield 0028, South Africa*
[2]*Department of Chemistry, University of Pretoria, Private Bag X20, Hatfield 0028, South Africa*

Corresponding author e-mail addresses: pannan.kyesmen@up.ac.za; mmantsae.diale@up.ac.za

Highlights

- Heterojunction structure of α-Fe_2O_3 with porous CuO enhanced PEC water splitting.
- Porous nanostructured CuO was prepared on α-Fe_2O_3 films using a new approach.
- 19 × more photocurrent at 1.0 V vs RHE recorded for α-Fe_2O_3/CuO compared to α-Fe_2O_3.
- The heterojunction and porous interface of α-Fe2O3/CuO enhanced charge separation.
- Reduced bandgap of α-Fe_2O_3/CuO improved light absorption and PEC water splitting.

Abstract

In this research, nanostructured heterojunction of hematite (α-Fe_2O_3) and porous copper (II) oxide (CuO) composites represented as α-Fe_2O_3/CuO was prepared and used as photoanode for photoelectrochemical (PEC) water splitting. X-ray diffraction (XRD) and Raman spectroscopy studies confirmed the high purity of α-Fe_2O_3/CuO heterostructures produced. Enhanced photocurrent density of 0.53 mA/cm^2 at 1.0 V versus reversible hydrogen electrode (vs. RHE) was achieved for α-Fe_2O_3/CuO photoanodes, representing a 19-fold increase compared to the value recorded for α-Fe_2O_3. The formation of a heterojunction coupled with the porous surface morphology of α-Fe_2O_3/CuO heterostructure facilitated charge separation of photogenerated electron-hole pairs, enhancing PEC water splitting. The reduced bandgap recorded for α-Fe_2O_3/CuO resulted in increased absorption of photon in the visible spectrum by the heterostructure, which also influenced the improvement of the photocurrent density. Furthermore, increase in charge carrier density and the reduction of charge transfer resistance at the liquid/solid interface achieved for α-Fe_2O_3/CuO were additional evidence associated with the improvement in the recorded current density. This research presents the formation of α-Fe_2O_3/CuO heterojunction structure with porous surface as a viable route to achieving notable improvement in the photo response of α-Fe_2O_3 photoanodes for PEC water splitting.

Keywords: α-Fe_2O_3, CuO, heterojunction structure, photocurrent, water splitting.

1 Introduction

In recent years, there has been an increasing global need for renewable energy sources in order to mitigate the environmental challenges associated with the burning of fossil foils. Solar energy is regarded as a renewable energy source, which is clean, abundant and can be harvested and stored as fuels in the form of hydrogen [1] and hydrocarbon compounds [2] via PEC water splitting and photoreduction of carbon dioxide respectively. The production of hydrogen through PEC water splitting has attracted the attention of researchers globally since its first

demonstration in 1972 by Fujishima and Honda [3]. Fujishima and Honda use TiO_2 as a semiconductor photoanode and achieved a low quantum efficiency of 0.1%. One reason for the low quantum efficiency was the inability of TiO_2 to absorb photons in the visible spectrum due to its large bandgap of 3.0 eV. Their research suggested the need to utilize semiconductors that are able to use the photons in the visible region and stable in aqueous media, for PEC water splitting. Over the years, semiconductors which are stable in aqueous solution and are able to harvest light in the visible spectrum such as $BiVO_4$, WO_3 and α-Fe_2O_3 have been vastly investigated for use as a photocatalyst for PEC water splitting [4]. Among these, α-Fe_2O_3 is one of the most investigated because it is capable of harvesting considerable number of photons in the visible spectrum because of its bandgap of ~2.0 eV [5] and theoretical solar to hydrogen (STH) efficiency of 17.0% [6]. However, the efficiency of α-Fe_2O_3 is yet to attain the theoretically predicted value due to its poor conductivity, short hole diffusion length leading to high electron-hole recombination and inefficient charge separation [7, 8].

Numerous approaches have been employed in dealing with the challenges associated with the use of hematite for PEC water splitting which include nanostructuring, doping, and the formation of heterojunction materials. Nanostructuring of hematite have been widely used to promote charge separation on films surfaces where water oxidation reaction occurs during photocatalysis [9]. Different nanostructured hematite with surface morphologies of nanoparticles [10], nanorods [11], nanotubes [12], and nanoflowers [13] among others have been reported to have played a role in improving charge carrier separation during photocatalysis. The concept of doping has also been utilized to boost the charge carrier density of hematite films thereby improving their conductivity leading to enhanced PEC efficiency. Doping of hematite with elements such as tin (Sn) [9], manganese (Mn) [14], and sulphur (S) [15] among others, have yielded improvement of photo response during water splitting. The formation of heterojunction structures is one promising approach that has been widely utilized to limit charge recombination, enhance charge separation and also improve photon absorption of hematite photocatalyst for efficient PEC water splitting [16-19].

The formation of a heterojunction can create an electric field at the interface that is formed between the heterostructures which can help to facilitate charge transport and separation as well as limit electron-hole recombination [4]. More so, a heterojunction allows for the incorporation of materials that can absorb photons at different wavelengths in the visible region, thereby increasing the number of photogenerated electron-holes pairs and PEC performance. Depending on the semiconductor materials used to form the heterostructure (n-type or p-type), an n-n, p-p or p-n junction structure could be formed. The p-n junction heterostructures is a commonly used architecture for PEC water splitting [20]. Several hematite base p-n junction heterostructures such as NiO/α-Fe_2O_3 [21], α-Fe_2O_3/Cu_2O [19], $CaFe_2O_4$/α-Fe_2O_3 [22] and α-Fe_2O_3/CuO [23] have been applied towards PEC water splitting. Besides the formation of a p-n heterojunction, α-Fe_2O_3/CuO can significantly enhance the absorption of photons in the visible spectrum because of the low bandgap of CuO given as 1.55 eV [24]. However, the use of α-Fe_2O_3/CuO heterostructure for PEC water splitting has been scarcely reported in literature. Pastrana *et al*. (2019) prepared α-Fe_2O_3/CuO heterostructures, used as photocatalyst for water splitting and reported a cathodic photocurrent density of -0.19 mA/cm^2 at 0.18 V vs RHE [23].

In this research, α-Fe_2O_3 and α-Fe_2O_3/CuO heterojunction photoanodes were prepared by dip coating and the enhancement of PEC water splitting resulting from the formation of the

heterostructure was studied. A new approach of preparing porous CuO developed in this project was used in formation of the heterostructure with α-Fe_2O_3.The photocurrent density recorded for α-Fe_2O_3/CuO at 1 V vs. RHE was 19-fold more than the value recorded for pristine hematite. The absorption onset of α-Fe_2O_3/CuO relative to that of α-Fe_2O_3 was red-shifted. This led to improved absorption of photons in the visible spectrum which influenced the enhancement in the photocurrent density achieved for α-Fe_2O_3/CuO photoanode. Also, the formation of α-Fe_2O_3/CuO heterojunction structure produced an in-built electric field at the p-n junction that facilitated the movement of photoexcited charge carriers which significantly reduced the recombination of electron-hole pairs and impacted positively on its water splitting capability. The morphology of CuO deposited on α-Fe_2O_3 to form the heterostructure was porous and may have played a significant role in boosting charge separation, and consequently photocatalytic efficiency. In addition, increased charge carrier density as well as the lowering of charge transfer resistance at the solid/liquid interface recorded for α-Fe_2O_3/CuO explained the enhancement of photocurrent density achieved.

2 Experimental

2.1 Preparation of α-Fe_2O_3 films

Hematite films were deposited on FTO substrates following a procedure that has been reported in detail elsewhere [25]. In summary, iron(III) *nitrate nonahydrate* ($Fe(NO_3)_3.9H_2O$) and oleic acid were mixed in a mass ratio of about 2:1 and heated for 2.5 hrs at 110°C to yield a red-brown mass. The mass was then treated with 80 mL of tetrahydrofuran, sonicated for 15 min with an ultrasonic bath and centrifuged for 3 mins at 5000 rpm. The supernatant solution collected was used for the deposition of hematite films on cleaned FTO substrates via the dip coating approach. In the dip coating process, the FTO substrate was immersed for 2 mins in the precursor, removed at a withdrawal rate of 30 mm/min, dried for 15 min at 70°C and annealed for 30 mins at 500°C. The process was repeated thrice to produce four layers of dip coated thin films of hematite.

2.2 Preparation of α-Fe_2O_3/CuO films

The α-Fe_2O_3 films prepared on FTO were used as the substrate for the deposition of porous CuO nanostructures to form α-Fe_2O_3/CuO heterojunction. The precursor used for the deposition of CuO was prepared by mixing 0.25 M copper acetate in 90% propan-2-ol, 5% diethanolamine and 5% polyethylene glycol 400.The copper acetate was first dissolved in propan-2-ol and stirred for 1 hr. Afterwards, diethanolamine was added and continuously stirred for another 1 hr. Finally, polyethylene glycol was poured into the solution in a dropwise manner and further stirred for 1 hr. The solution obtained was aged for 70 days and used as the precursor solution for the deposition of CuO films. The α-Fe_2O_3 films prepared on FTO was immersed into the solution for 60 s, withdrawn at the rate of 1 mm/s and dried using a two-step method; at 110°C and 250°C for 10 and 5 min respectively. The dip coating process was repeated twice after which the films were introduced into the furnace at 300°C, heated to 550°C at the rate of 10°C/min and annealed at that temperature for 1 hr. Thereafter, the films were left to cool down to room temperature naturally producing a heterojunction structure of α-Fe_2O_3/CuO films. Fig. 1 presents a chart that summarizes the procedure for the preparation of

CuO on FTO/α-Fe_2O_3 films. Following the same procedure, CuO films were prepared on FTO substrates for comparative purpose.

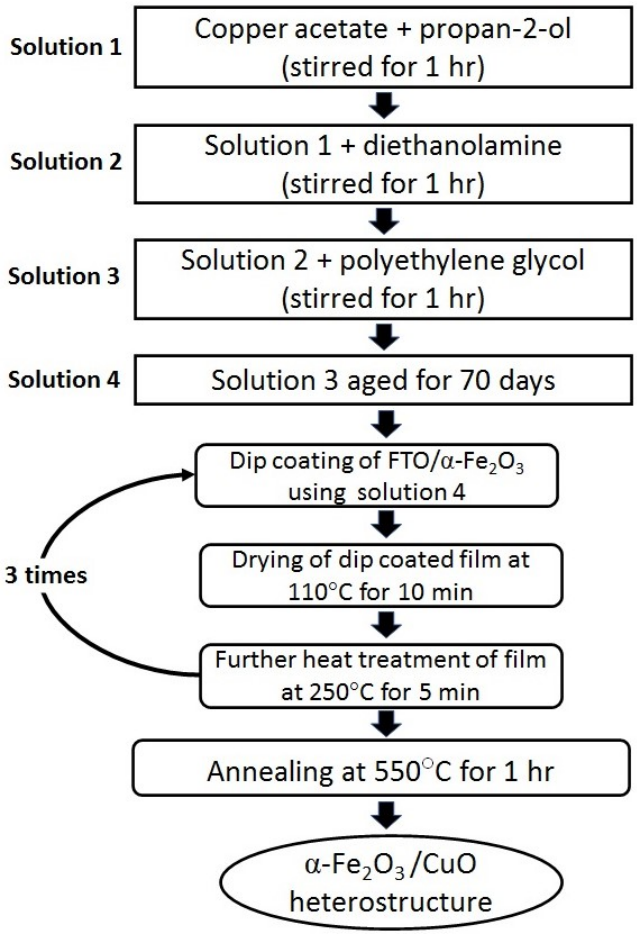

Fig. 1. A chart showing the summary of the procedure used for the preparation α-Fe_2O_3/CuO heterostructure.

2.3 Characterization

XRD technique was employed to investigate the structural properties of pristine α-Fe_2O_3, CuO and α-Fe_2O_3/CuO films Bruker D2 PHASER-e diffractometer of Cu-Kα radiation at wavelength of 0.15418 nm. Zeiss Ultrafast 540 instrument was used to examine morphology of the films by field emission gun scanning electron microscopy (FEG-SEM). The cross-section view of α-Fe_2O_3/CuO film was also examined using FEG-SEM to obtain approximate film thickness of the composite materials in the heterostructure. Energy dispersive X-ray Spectroscopy (EDS) which is coupled to the Zeiss Ultrafast 540 instrument was engaged to study the constituent elements in the films as well as the chemical distribution across the cross-section of α-Fe_2O_3/CuO heterostructure. The optical properties of the films were examined using CARY 100 BIO Ultraviolet-Visible (UV-Vis) spectrometer. Raman spectroscopy study of the films were performed using a WiTec alpha300 RAS+ Confocal Raman Microscope with excitation laser of 532 nm at 5 mW.

2.4 PEC measurements

The pristine α-Fe_2O_3, CuO and α-Fe_2O_3/CuO films produced were used as photocatalyst in a three-electrode electrochemical system and their PEC properties were studied. The electrochemical cell consists of Na_2SO_4 as the electrolyte (pH=5.8) while the photoelectrodes, 2 × 2 cm platinum mesh and Ag/AgCl in 3M of KCl were utilized as the working, counter and reference electrodes respectively. VersaSTAT 3F potentiostat from Princeton Applied Research coupled to the electrochemical cell was used to carry out the PEC measurements. Voltammetry scan was performed on the films in dark and under illumination at the scan rate of 50 mV/s to observe their photocurrent response. Newport $Oriel^{®}\ LCS\ -\ 100^{TM}$ solar simulator was calibrated using a Newport 91150V reference cell to 1 sun and utilized as the light source. The surface area of the photoelectrodes exposed to illumination was 0.49 cm^2. Electrochemical impedance spectroscopy (EIS) measurements were performed on the photoanodes under dark conditions at 0.5 V vs. Ag/AgCl, frequency range of 10, 000 - 0.1 Hz and at an excitation amplitude of 10 mV. Furthermore, EIS was conducted on α-Fe_2O_3/CuO in Na_2SO_4 electrolyte containing 15% methanol (pH=5.8) as sacrificial reagent (SR). The EIS experimental data obtained was fitted to an equivalent circuit model using the ZView software purchased from Scribner Associates. Mott-Schottky analysis were performed on the films under dark conditions at a single frequency of 1000 Hz, AC potential amplitude of 10 mV and a DC potential interval of -1.0 to 1.0 V vs. Ag/AgCl. Chronoamperometry measurement were performed on the photoanodes at 0.5 V vs. Ag/AgCl to investigate their stability in electrolyte. The potential against Ag/AgCl reference were all converted to RHE scale using the Nernst equation:

$$V_{RHE} = V_{Ag/AgCl} + (0.059 \times pH) + 0.1976\ V \quad (1)$$

where, V_{RHE} is the potential in RHE scale, 0.1976 V is the value of Ag/AgCl reference electrode standard potential vs. NHE at 25°C, and $V_{Ag/AgCl}$ represents the potential used in the experiment against Ag/AgCl reference electrode [26, 27].

3 Results and discussion

3.1 Structural properties

XRD study was performed on the films prepared to obtain information on their structural properties. Fig. 2 shows the XRD pattern for α-Fe_2O_3, CuO and α-Fe_2O_3/CuO film. The XRD pattern for α-Fe_2O_3 films revealed diffraction peaks at (110) and (104) planes which indicates that hematite's rhombohedral crystal structure with lattice parameters a = b = 5.032, c = 13.733; $R\bar{3}c$ space group has been formed. The pattern also revealed weak reflections at (012), (113), (024), (122) and (310) planes corelating with those of α-Fe_2O_3 according to the JCPDS file no. 33-0664. Other forms of iron oxide were not observed, confirming high quality of prepared α-Fe_2O_3 films. The diffraction pattern of CuO films revealed peaks at $(\bar{1}11)$ and (111) planes which is indexed to the monoclinic crystal structure with lattice parameters *a* = 4.64 Å, *b* = 3.4 Å, *c* = 5.09 Å, β = 99.5° according to JCPDS no 05-0661. Bragg reflections for copper (Cu) and copper (I) oxide (Cu_2O) were not observed, confirming high purity of CuO. The XRD pattern for α-Fe_2O_3/CuO confirmed the presence of the composite materials with the detection of the diffraction peaks observed for both α-Fe_2O_3 and CuO films.

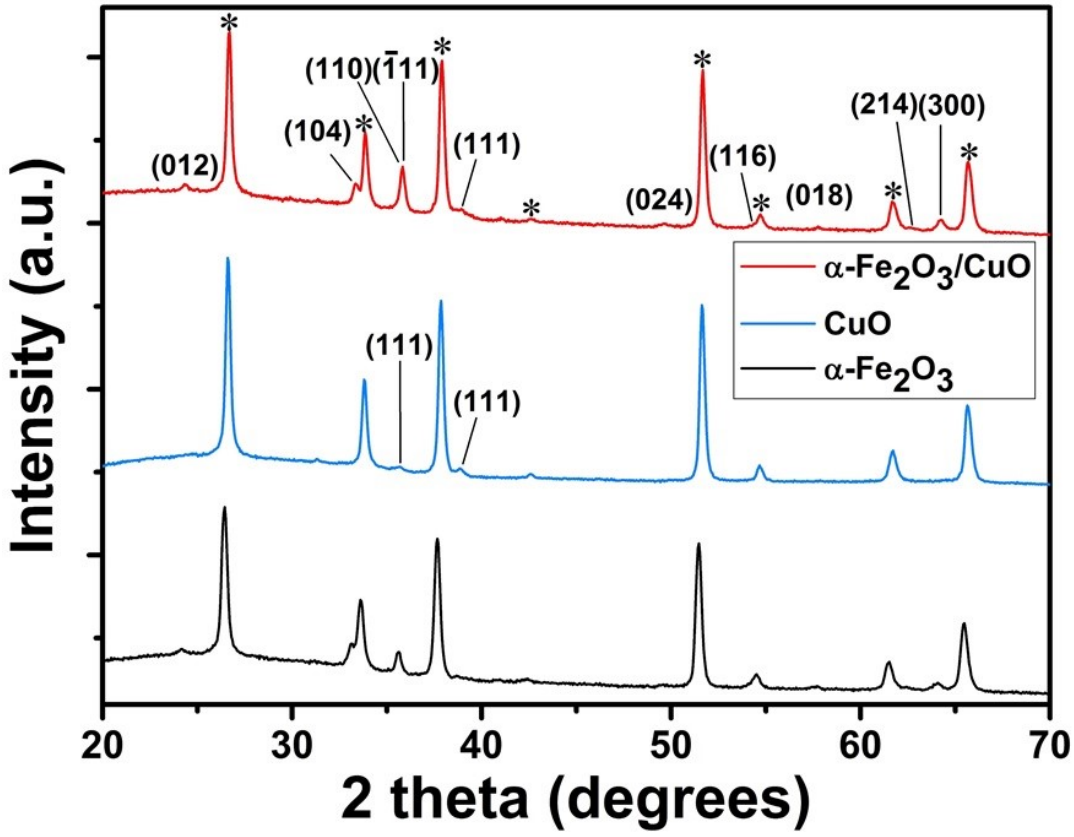

Fig. 2. XRD pattern of α-Fe_2O_3, CuO and α-Fe_2O_3/CuO films. Note: the * symbol represent the XRD peaks of FTO substrates.

A shift of about 0.173 and 0.186° towards higher 2θ values was observed for the (104) and (110) peaks of the α-Fe_2O_3/CuO heterostructure relative to that of α-Fe_2O_3 respectively, as shown in Fig. S1 of the supplementary data. The shift may have been caused by unintentional doping of α-Fe_2O_3 through the diffusion of some Cu ions into α-Fe_2O_3 during the annealing process of the Cu-based precursor to form the heterostructure. Depending on the preparation process of doped hematite, the lattice volume may increase or decrease causing the XRD peaks to shift to lower or higher 2θ values respectively [28]. XRD peak shifts to lower [13, 29, 30] and higher [28, 31] 2θ values have been observed in literature for Cu doped α-Fe_2O_3. The XRD peak shifts observed for α-Fe_2O_3 in the heterostructure may have been caused by the reduction of lattice size due to the doping effect. The substitution of Fe^{3+} by Cu^{2+} can result in charge imbalance and for charge neutrality, some oxygen vacancies are created causing a reduction in the lattice size and the shift of XRD peaks to higher 2θ values [28, 31].

Furthermore, additional structural information was obtained by characterizing α-Fe_2O_3, CuO and α-Fe_2O_3/CuO composite using Raman spectroscopy; a probe that is sensitive to the phonon vibrations in materials. Raman scattering gives information on the bonds of a material and is able to ascertain the presence of unwanted phases such as magnetite (Fe_3O_4) and Cu_2O in α-Fe_2O_3 and CuO respectively [32]. The Raman spectra of the films studied are presented in Fig. 3. The spectra for the α-Fe_2O_3 films confirmed the $2A_{1g}$ and $5E_g$ vibrational phonon modes of

the films. The peaks observed at 230 and 504 cm^{-1} have been indexed to the A_{1g} modes while the ones at 250, 297, 305, 414, 614 cm^{-1} are alloted to the E_g modes, similar to what has been reported for α-Fe_2O_3 in literature [33]. The phonon modes belonging to Fe_3O_4 or other forms of iron oxide were not detected, confirming high purity of the produced hematite films. The spectra for CuO films revealed the $2B_g$ and $1A_g$ Raman active phonon modes for the films. The peak at 302 cm^{-1} is indexed to the Ag mode and ones at 250 and 638 cm^{-1} are assigned to the B_g modes. The phonon modes belonging to copper (Cu) or other forms of copper oxide were not detected, confirming high quality of the CuO films prepared. The spectra of α-Fe_2O_3/CuO composite revealed all the phonon vibrational modes detected for both α-Fe_2O_3 and CuO further confirming the composite materials in the heterostructure. The peaks at 302, 297 and 305 cm^{-1} for A_g and $2E_g$ modes of CuO and α-Fe_2O_3 respectively overlapped with each other resulting to a single peak been observed in the Raman spectra of the α-Fe_2O_3/CuO heterostructure.

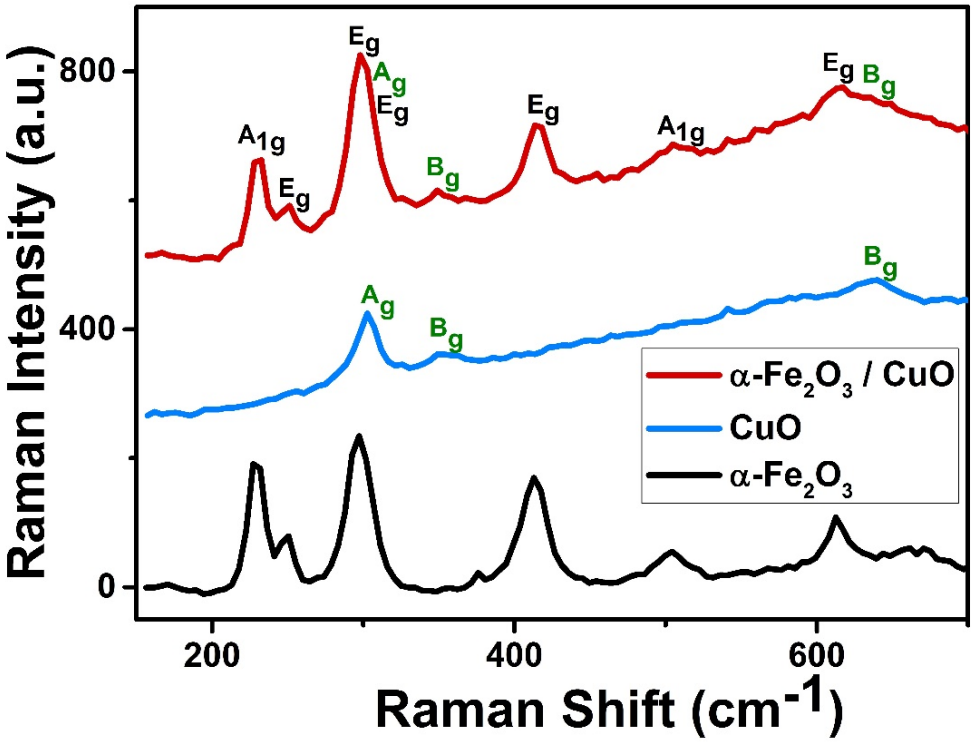

Fig. 3. Raman spectra of α-Fe_2O_3, CuO and α-Fe_2O_3/CuO films.

The Raman intensities of the vibrational phonon modes of α-Fe_2O_3 in the spectra of α-Fe_2O_3/CuO decreases relative to those of pristine α-Fe_2O_3, as clearly shown in Fig. S2 of the supplementation data. The decreased Raman intensities is attributed to lattice distortions and reduce crystallization of α-Fe_2O_3 films that may have resulted from the unintentional doping of α-Fe_2O_3/CuO by Cu during the heat treatment of Cu-based precursor to form the heterostructure [34, 35]. The substitution of Fe^{3+} by Cu^{2+} will lead to the creation of oxygen vacancies to compensate for the resulting charge imbalance, decreasing the lattice volume and crystal size of the films [28, 31]. Reduction in crystal size of nanostructured materials has been linked with decreasing Raman peaks intensities in previous studies [36, 37]. The indication of Cu doping from Raman spectra analysis further support the claim in XRD analysis.

3.2 Morphology and elemental composition

Surface morphology of pristine α-Fe_2O_3, α-Fe_2O_3/CuO and CuO were characterized using FEG-SEM and the results are given in Fig. 4 (a), (b) and (c) respectively. The morphology of the hematite films revealed some larva-shaped and spherical nanostructures. The larva-shaped nanostructures may have resulted from the agglomeration of some of the spherical nanoparticles. The α-Fe_2O_3/CuO revealed spherical nanoparticles for CuO at the film's surface which are porous and more inhomogeneous compared to the α-Fe_2O_3 films. FEG-SEM analysis was carried out on CuO films prepared on FTO in order to understand the influenced of using FTO/α-Fe_2O_3 substrate on the surface morphology observed for α-Fe_2O_3/CuO heterostructure. The morphology of pure CuO nanostructures revealed porous surface and spherical particles that are similar with those of α-Fe_2O_3/CuO. This indicates that the FTO/α-Fe_2O_3 used to prepare α-Fe_2O_3/CuO composite did not influence the surface morphology observed. The particle diameter of the nanostructures of the samples were estimated using ImageJ software. The particle size estimated for α-Fe_2O_3, CuO and α-Fe_2O_3/CuO nanostructures were 35.3, 37.3 and 38.8 nm with standard deviation of 6.1, 6.2 and 7.0 nm respectively. The histogram of the particle size distribution of the α-Fe_2O_3, CuO, α-Fe_2O_3/CuO nanostructures are presented in Fig. S3 of the electronic supplementary information. The difference in the particle size of α-Fe_2O_3 and α-Fe_2O_3/CuO was not quite significant and may have no influence on PEC performance. However, the porous nature of α-Fe_2O_3/CuO surface can be helpful in enhancing charge separation during PEC water splitting and consequently its performance [38].

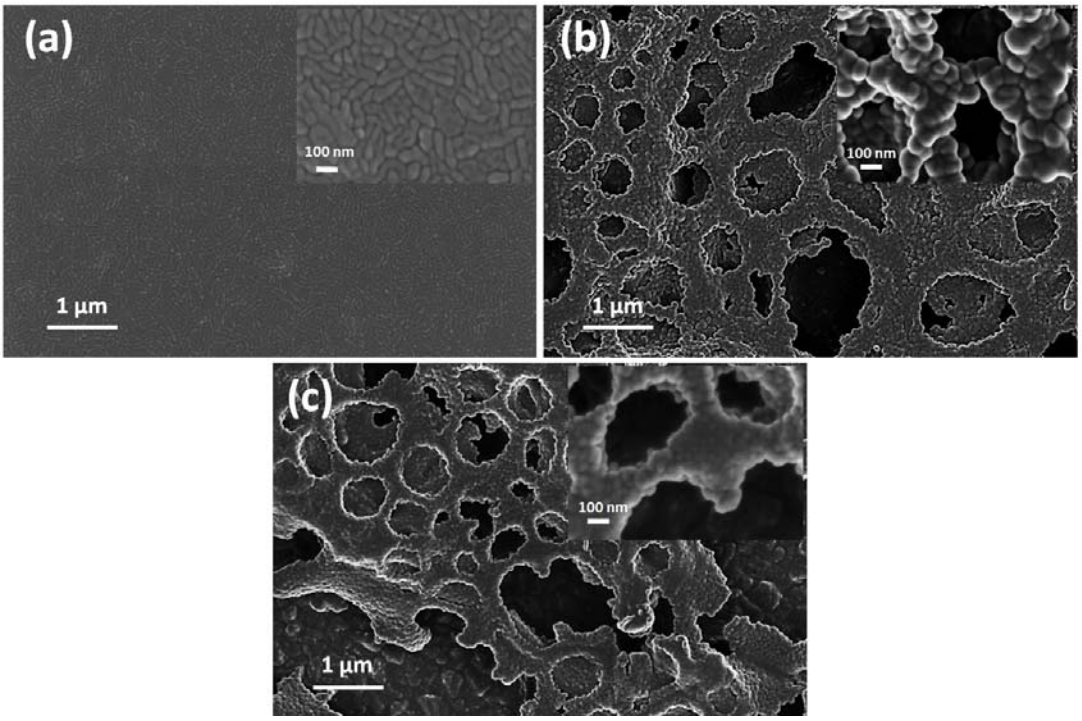

Fig. 4. Surface micrographs of (a) α-Fe_2O_3, (b) α-Fe_2O_3/CuO and (c) CuO films: with the insets showing their images at higher magnifications respectively.

The cross-sectional image of the α-Fe_2O_3/CuO was investigated to obtain the estimated film thickness of the composite materials in the heterostructure. The cross-sectional view of the α-

Fe_2O_3/CuO composite is presented in Fig. 5(a). Film thickness of 425 ± 26 and 133 ± 16 nm were estimated for the α-Fe_2O_3 and CuO layers of the heterostructures respectively. α-Fe_2O_3 requires film thickness of about 400-500 nm for complete complete absorption because of its poor absorption coefficient [39]. This gives an indication that the total film thickness of 558 ± 42 nm recorded for the heterostructure may be effective for light absorption for PEC applications. The cross-section showed uniform distribution of CuO on α-Fe_2O_3 and a distinct junction formation at the interface between them.

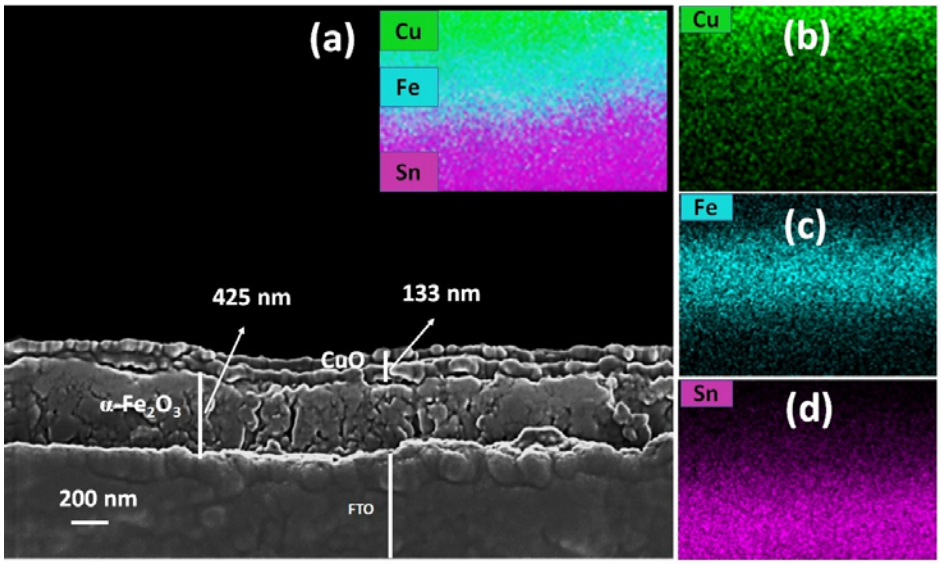

Fig. 5. (a) cross-sectional view of α-Fe_2O_3/CuO films with the inset showing corresponding EDS mapping: (b), (c) and (d) shows the signal distribution of the mapping for Cu, Fe and Sn respectively.

EDS mapping was carried out on the SEM cross-section of α-Fe_2O_3/CuO to ascertain elemental distribution in the core of the heterostructure. The inset of Fig. 5 (a) shows the EDS elemental mapping on the SEM cross-section while (b), (c) and (d) disclosed the signal distribution for tin (Sn), iron (Fe) and copper (Cu) across the map, respectively. A strong signal for Sn was noticed at the edge of the films, towards the substrate. This is a confirmation of the FTO substrate used for film deposition which contains Sn as one of its constituent elements. A well pronounced signal of Fe was noticed after that of Sn indicating the formation of α-Fe_2O_3 films on FTO. The distribution of Cu was observed on the surface of the films indicating the formation of CuO on α-Fe_2O_3 to form α-Fe_2O_3/CuO heterostructure. The results of the EDS measurement performed on the surface morphology of α-Fe_2O_3/CuO is given in Fig. S4 of the electronic supplementary information. Oxygen (O), Fe, Cu and silicon (Si) were detected in the analysis. Hight content of O was detected in the analysis due to its presence in SnO, α-Fe_2O_3, and CuO which made up the entire sample. Fe was detected due to its presence in α-Fe_2O_3 films. The presence of Cu resulted from the formation of CuO on the surface of α-Fe_2O_3 while Silicon (Si) was detected due to the quarts contend of glass from the glass/FTO substrates used.

3.3 Optical properties

Optical studies were performed on the films using UV-Vis spectroscopy to analyse the absorption pattern and the bandgaps of the films. The absorption spectra of α-Fe_2O_3 and α-Fe_2O_3/CuO films are presented in Fig. 6(a). The absorption peak obtained for hematite at 390 nm got red-shifted to 412 nm by the α-Fe_2O_3/CuO heterostructure. The difference in the band gap of α-Fe_2O_3 and CuO will cause the realignment of the conduction band (CB) and valence band (VB) in the energy band structure of α-Fe_2O_3/CuO resulting in the red-shift observed for the absorption spectra of the heterostructure [40]. In addition, the grain boundaries at the interface formed between the composite materials will lead to the generation of many intermediate energy levels below the CB of α-Fe_2O_3 allowing for easier movement of electrons from the VB to the CB of the heterostructure [41, 42]. This will lead to improve absorption in the visible spectrum by the heterostructure which is significant for improving PEC performance [43].

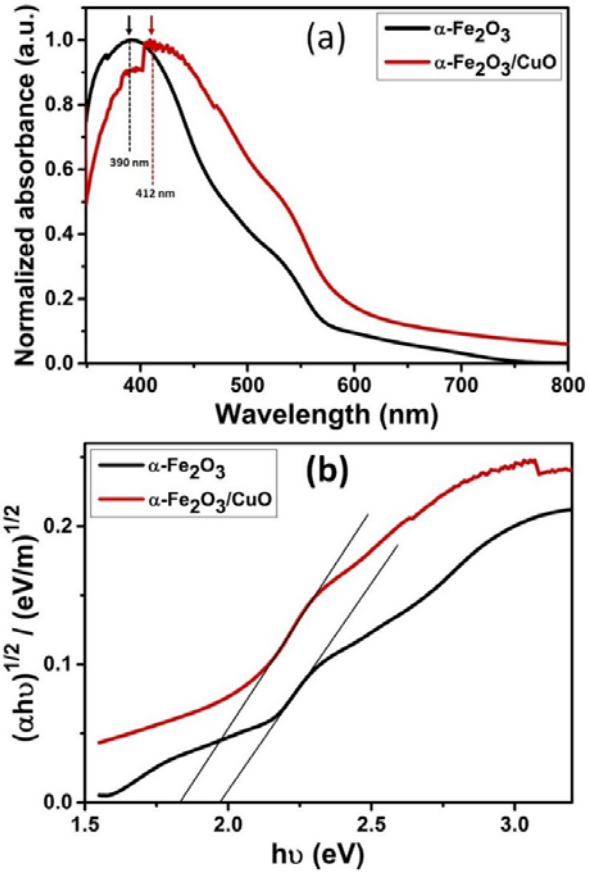

Fig. 6. A plot of (a) UV-Vis normalized absorption spectra and (b) Tauc approximation for indirect bandgaps of α-Fe_2O_3 and α-Fe_2O_3/CuO films.

From the absorption spectra of α-Fe_2O_3 and α-Fe_2O_3/CuO, the approximate optical bandgaps of the films were extracted from the Tauc plots for indirect transitions shown in Fig. 6(b). The estimated optical bandgap for α-Fe_2O_3 and α-Fe_2O_3/CuO films were approximately 1.98 and 1.83 eV respectively. The reduced bandgap of α-Fe_2O_3/CuO resulted to the red-shifting of its absorption onset relative to that of α-Fe_2O_3. This led to the improved photon absorption in the

visible spectrum observed for α-Fe_2O_3/CuO which will enhance the number of photogenerated electron-hole pairs in the films during PEC water splitting and consequently enhance performance.

3.4 Photoelectrochemical properties

Linear sweep voltammetry measurements were done under dark and illumination conditions on the α-Fe_2O_3 and α-Fe_2O_3/CuO photoelectrodes to obtain their photocurrent response. Fig. 7(a) presents the results of the voltammetry scan done on the photoelectrodes under dark conditions. Dark current density of 0.1 mA/cm^2 was observed at 1 V vs. RHE for α-Fe_2O_3/CuO films whereas no noticeable value was recorded for α-Fe_2O_3 film at the same reference potential. The improved dark current was caused by improved charge transport in the heterostructure and slower recombination of charge carrier's due to the large surface area of the porous α-Fe_2O_3/CuO interface, which will provide more active sites for water oxidation [44]. Improvement in charge transport in the bulk of the films due the formation of the heterojunction structure will allow for more holes to get to the surface of the films where water oxidation occurs [1, 45]. In the presence of increased number of holes at the solid/liquid interface, slower recombination of charge carrier's due to the increased interfacial surface area will improve the extraction of holes for water oxidation, increasing the dark current [44, 46, 47]. Similar large dark current has been reported for α-Fe_2O_3/NiO where the solid/liquid interface consist of nanowires providing large surface area for water oxidation [44].

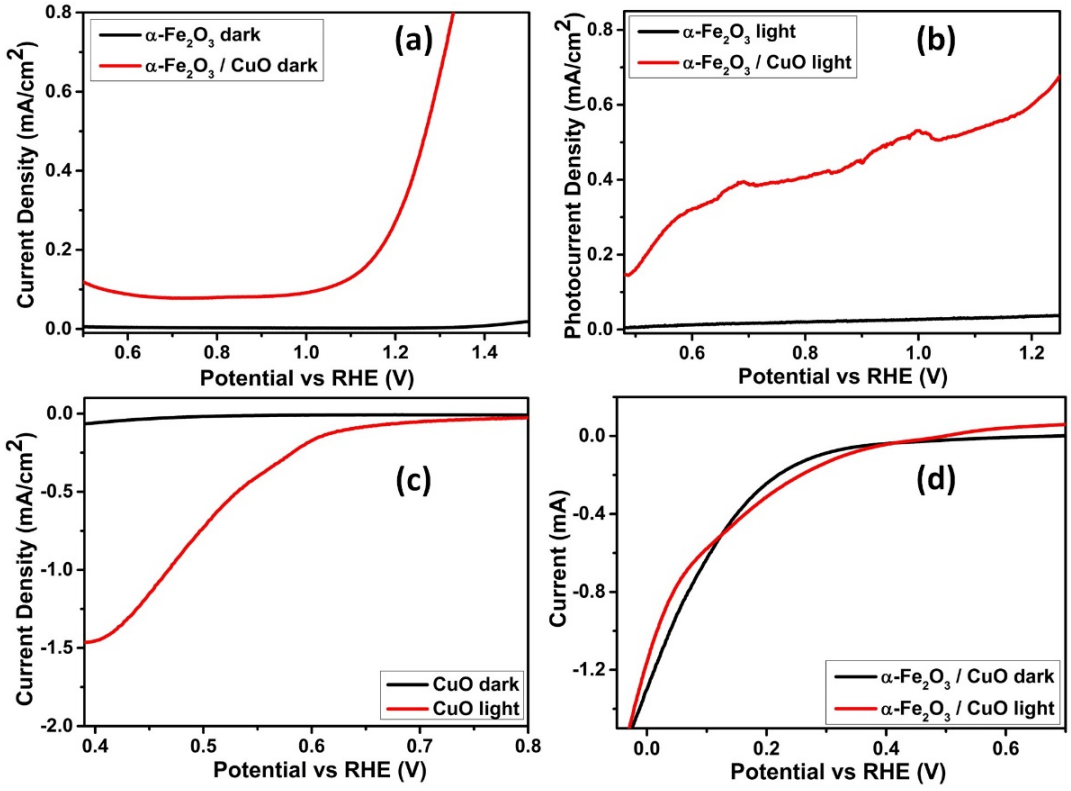

Fig. 7. Current density for α-Fe_2O_3 and α-Fe_2O_3/CuO photoanodes for measurements done under (a) dark and (b) illumination conditions: (c) and (d) shows the cathodic current response of CuO and α-Fe_2O_3/CuO films respectively.

Photocurrent density is one of the direct parameters that reflects the PEC performance of photoelectrodes [4]. Fig. 7(b) presents the current response of α-Fe_2O_3 and α-Fe_2O_3/CuO for measurements done under illumination. Photocurrent density of 0.53 mA/cm^2 at 1 V vs. RHE was recorded for α-Fe_2O_3/CuO, representing a 19-fold increase compared to the value obtained for α-Fe_2O_3 photoanodes (0.027 mA/cm^2). The formation of a heterojunction structure produced an in-built electric field at the p-n junction that facilitated the movement of photoexcited charge carriers which significantly reduced recombination of electron-hole pairs, leading to the improved photocurrent observed [45]. The reduction in the optical bandgap observed for α-Fe_2O_3/CuO enhanced its photon absorption in the visible region, increasing the number of photogenerated electron-hole pairs thereby contributing to the improved photocurrent response achieved [43]. Also, the porous nature of the films surface for α-Fe_2O_3/CuO may have helped in enhancing charge separation and the photo response recorded for the films [38]. In addition, the unintentional doping of α-Fe_2O_3 by Cu during the heat treatment of Cu-based films to form α-Fe_2O_3/CuO as explained in section 3.1 can improve the conductivity and enhanced charge transport, contributing to the increased photocurrent response of the heterostructure [13, 30]. In order to observe the cathodic current response of CuO and α-Fe_2O_3/CuO films, a negative voltammetry scan was conducted and the results are presented in Fig. 7(c) and (d) respectively. CuO been a p-type semiconductor produced a cathodic photocurrent of -1.15 mA/cm^2 at 0.45 V vs. RHE. However, no noticeable cathodic photocurrent was observed for α-Fe_2O_3/CuO, indicating that the heterostructure possesses an n-type property, further validating the anodic current response observed for the films.

The mechanism of PEC water oxidation using heterojunction materials has been reported in previous literature [45, 48-50]. In summary, if a heterostructure is formed between a p-type and an n-type semiconductor material, a space charge layer is created at the interface between them. The formation of the space charge layer is caused by the diffusion of majority charge carriers from the p-type and n-type materials in opposite direction, leading to the creation of a p-n junction and an electric field at the interface of the semiconductors [45]. Depending on the position of the valence band (VB), conduction band (CB) and fermi level of the semiconductor materials, the energy diagram and charge transfer process of the heterostructure can be illustrated. Fig. 8 present an illustration of the charge transfer process and energy diagram of α-Fe_2O_3/CuO heterostructure. The optical band gap estimated for α-Fe_2O_3 is ~2.0 eV while the calculated VB and CB edges has been reported as 0.3-0.6 and 2.4-2.7 eV respectively. The approximate bandgap for CuO is 1.55 eV with VB and CB edge values as -0.51 and 1.04 eV respectively [24]. The CB edge for CuO is higher compared to that of α-Fe_2O_3 while its Fermi energy level is lower and less negative [23]. Upon formation of α-Fe_2O_3/CuO heterostructure, the fermi levels will adjust and achieve equilibrium through the diffusion of majority charge carries from each of the semiconductors as earlier explained. This will lead to the creation of space charge layer, an internal electric field and energy band bending at the interface joining the α-Fe_2O_3/CuO composites as shown in Fig 8. Upon photoexcitation of α-Fe_2O_3/CuO, the photogenerated holes from the VB of α-Fe_2O_3 are moved to that of CuO which then goes on to perform water oxidation at the solid/liquid interface. Also, photogenerated electrons from the CB of CuO is transferred to that of α-Fe_2O_3. The electrons in the CB of α-Fe_2O_3 are then transferred to FTO from where they move to the counter electrode through the back contact to reduce H^+ into H_2. The movement of photoexcited holes and electrons between α-Fe_2O_3 and CuO is facilitated by the electric field at the p-n junction enhancing effective charge separation and significantly reducing recombination of electron-hole pairs [1, 45]. This served a critical role in enhancing the photocurrent density recorded for α-Fe_2O_3/CuO relative to that of α-Fe_2O_3 photoanodes.

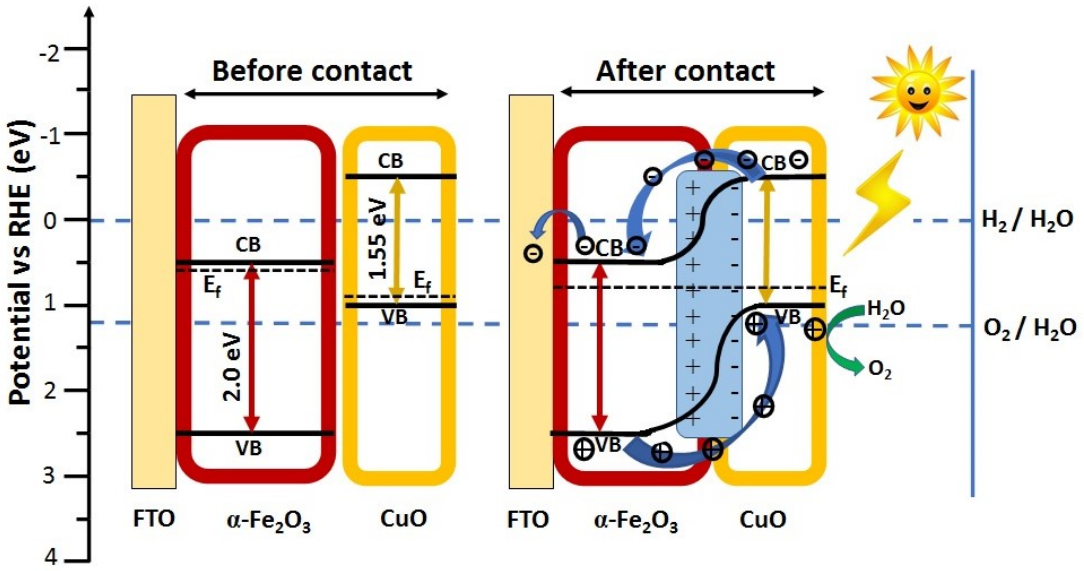

Fig. 8. Energy diagram and charge transfer processes for α-Fe_2O_3/CuO heterojunction structure.

Additional reasons behind the improved photo response recorded for α-Fe_2O_3/CuO heterojunction material over α-Fe_2O_3 was extracted from the EIS studies of the photoanodes. EIS was engaged to study the charge transport processes occurring at the surface and bulk of the films. Fig. 9. shows the Nyquist plots of the EIS measurements done on α-Fe_2O_3 and α-Fe_2O_3/CuO photoanodes. The equivalent circuit model used to fit the experimental data obtained is presented in the inset of Fig. 9. The Rs in the circuit model stand for the series resistance due to FTO, the electrolyte and the conducting wires of the external circuit [51, 52]. In the two RC-circuits of the model, Rb and the constant phase element 1 (CPE1) stands for the charge transport resistance and the space charge capacitance in the bulk of the films while Rct and CPE2 represents the charge transfer resistance and the capacitance of the double layer at the surface of the photoanodes respectively. CPE was used to represent capacitive behaviours. This is because the inhomogeneous nature of the films surface as revealed in their morphology will result to a capacitive behaviour that is non-ideal [53].

The values obtain for the circuit components after fitting of the raw experimental data to the modelled circuit are given in Fig. 9(b). In the bulk of the films, charge transport resistance decreased while the space charge capacitance significantly increased for α-Fe_2O_3/CuO relative to α-Fe_2O_3 photoanodes. Lowered charge transport resistance and increased capacitance in the bulk of α-Fe_2O_3/CuO can result to easier movement of photogenerated holes to the surface of the films where water oxygen reaction takes place. At the surface of the films, the charge transfer resistance notably reduced for α-Fe_2O_3/CuO by a factor of about 29 and the double layer capacitance increased by over 6 times compared to the value recorded for α-Fe_2O_3, respectively. The significant reduction of charge transfer resistance achieved have been associated to two main factors. First, the electric field developed at the interface of α-Fe_2O_3/CuO due to the formation of a heterojunction structure significantly supports charge transport and decreased recombination of electron-hole pairs, leading to decreased charge transfer resistance [45]. Secondly, the porous surface of the α-Fe_2O_3/CuO provided a larger contact area with more active sites for OER at the photoanode/electrolyte interface which

significantly improved interfacial charge transfer, leading to the reduced Rct value recorded [38]. The reduced charge transfer resistance and increased capacitance of the double layer recorded for α-Fe_2O_3/CuO photoanodes is linked to the improvement in photocurrent density achieved for the films over those of α-Fe_2O_3. Similar observation has been reported for other heterostructure materials in literature [1, 54-56]. The use of 15% of methanol in the electrolyte as SR further resulted in a drop in the Rct value of the α-Fe_2O_3/CuO photoanode by 73.3%. This is an indication of further improvement in charge separation efficiency at the photoanode/electrolyte interface due to the presence of SR in the electrolyte acting as hole scavengers. More so, the electric field at the interface between the heterostructure allowed for more holes to get to the surface which are easily separated in the presence of SR, further confirming the suppression of charge recombination by α-Fe_2O_3/CuO relative to α-Fe_2O_3.

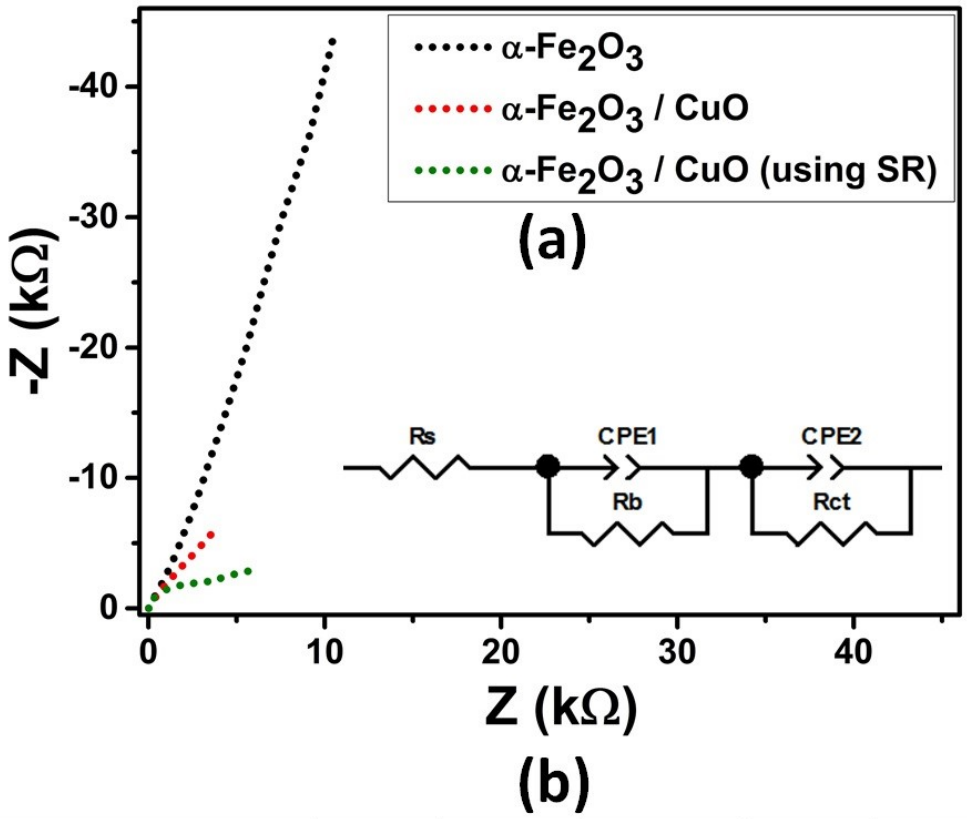

Sample	Rs (Ω)	Rb (kΩ)	CPE1 (μF)	Rct kΩ	CPE2 (μF)
α-Fe_2O_3	15.29	2.25	55.99	850	34.03
α-Fe_2O_3/CuO	15.19	1.68	240.62	29.6	226.05
α-Fe_2O_3/CuO using SR	17.14	3.19	33.21	8.0	228.33

Fig. 9. (a) the Nyquist plot for EIS measurements done on α-Fe_2O_3 and α-Fe_2O_3/CuO and α-Fe_2O_3/CuO (using 15% methanol as SR in the electrolyte) with the modelled circuit employed to fit the raw data presented in the inset and (b) shows the recorded values for the circuit elements used in fitting the data.

The Bode plot of log frequency (Hz) vs. phase (°) delay presented in Fig. S6(b) of the supplementary information was used to estimate the electron lifetime (τ_e) of the films using the

relation $\tau_e = 1/2\pi f_{max}$ where f_{max} represents the peak frequency [57, 58]. The f_{max} recorded for α-Fe_2O_3 and α-Fe_2O_3/CuO was 12.6 and 100.0 Hz corresponding to lifetimes of 1.6 and 12.6 ms respectively. The lifetime of α-Fe_2O_3/CuO increased by 7.9-fold compared to that of α-Fe_2O_3 suggesting a significant improvement in charge carriers transport due to the formation of the heterojunction structure.

In order to relate the donor density (N_D) and the position of the flat band potentials (V_{fb}) of the photoanodes with their photocurrent response, Mott-Schottky measurements were done on the films. Fig 10(a) shows the results of the Mott-Schottky investigation done on the photoanodes. The positive slope obtained for α-Fe_2O_3 and α-Fe_2O_3-CuO confirmed their properties as n-type materials and justifies their photoanodic response [59, 60]. The Mott-Schottky measurement done on CuO film shown in Fig 10 (b) yielded a negative slope, an indication of its p-type property [61]. This further validates the n-type behaviour observed for the α-Fe_2O_3/CuO heterostructure. The Mott-Schottky relation for an n-type material given in equation 2 was used to calculate the Nd and V_{fb} values for the photoanodes.

$$\frac{1}{C^2} = \frac{2}{\varepsilon_0 \varepsilon e A^2 N_D} \left(V - V_{fb} - \frac{KT}{e}\right) \quad (2)$$

where e denotes the electronic charge, K represents the Boltzmann constant, T denote the temperature, V stands for the applied potential, A is the electrode's surface area, Ɛ denotes the dielectric constant whose value is 80 for hematite, ε_0 denote the vacuum's permittivity, and C denotes the capacitance of the space charge layer [62]. In line with equation 2, the N_D values for the photoanodes where calculated using equation 3. The value of A used for each of the electrodes was about 1.8 cm^2: the surface area of the photoanodes dipped into the electrolyte.

$$N_D = \frac{2}{\varepsilon_0 \varepsilon e A^2} \left[\frac{dV}{d\left(\frac{1}{C^2}\right)}\right] \quad (3)$$

The donor density calculated for α-Fe_2O_3/CuO (1.75×10^{20} cm^{-3}) was 3.9 times more than the value obtained for α-Fe_2O_3 (4.5×10^{19} cm^{-3}). The increased in N_D for α-Fe_2O_3/CuO photoanodes was an indication of reduced charge recombination resulting from the formation of a heterojunction structure [63]. The reduced Rct value obtained for α-Fe_2O_3/CuO relative to that of α-Fe_2O_3 as presented in Fig. 9(b) is an indication of the decrease charge recombination which contributed to the increased N_D value observed. A similar trend of reduce charge recombination was observed for α-Fe_2O_3/CuO when 15% methanol was used as sacrificial reagent in the electrolyte resulting in further drop in Rct value by a factor of about 0.73 (Fig. 9(b)). This further confirmed the suppression of charge recombination by the heterostructure which contributed to the increased N_D value obtained for α-Fe_2O_3/CuO. Similar increase in donor density for p-n junction heterostructure materials have been observed in other studies [4, 45]. In addition, possible doping of α-Fe_2O_3 by Cu during the annealing of the Cu-based films to form α-Fe_2O_3/CuO may have contributed to the increased donor density obtained for the heterostructure [14, 64]. The improvement in donor density contributed to the enhance photocurrent density recorded for α-Fe_2O_3/CuO films.

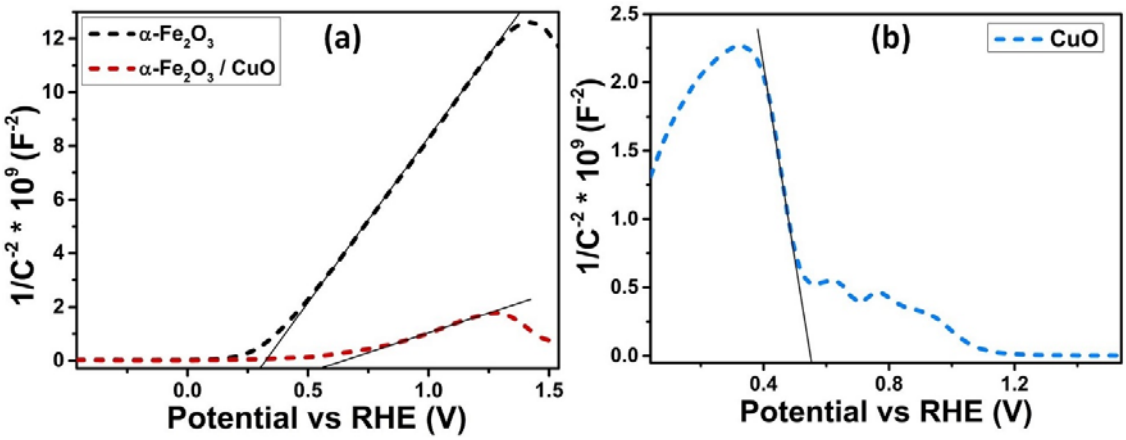

Fig. 10. Mott-Schottky analysis for (a) α-Fe_2O_3 and α-Fe_2O_3/CuO, and (b) CuO films.

The V_{fb} of the photoanodes were obtained through fitting the linear part of the MS plots, and using their intercept on the potential axis at $1/C^2 = 0$ to estimate the V_{fb} values. The flat band potential shifted positively from 0.30 V vs. RHE for α-Fe_2O_3 to 0.64 V vs. RHE for α-Fe_2O_3/CuO photoanodes. Since fermi level of CuO is less negative than that of α-Fe_2O_3 [23], the formation of heterojunction by the two semiconductors pulled the equilibrated fermi level to a more positive direction relative to that of α-Fe_2O_3 resulting in the flat band potential shift observed [65]. Similar positive shifts in V_{fb} for heterojunction materials have been reported in previous studies [55, 65]. The positive shift of V_{fb} is accompanied by the formation of an electric field at the interface between α-Fe_2O_3/CuO heterojunction which supports charge transport and limit recombination of electron-hole pairs.

Chronoamperometry measurement was performed on the α-Fe_2O_3 and α-Fe_2O_3/CuO films to study their stability in 0.5M Na_2SO_4 electrolyte. Hematite films shows good stability in the electrolyte during a current-time scan of 100 s, consistent with other observations in literature [6, 66]. The α-Fe_2O_3/CuO films was relatively unstable in electrolyte retaining 49.1 and 25.7% of it's photocurrent after 50 and 100 s respectively. The instability of α-Fe_2O_3/CuO films in electrolyte is attributed to photocorrosion of the CuO films deposited on the surface of the heterostructure [67]. The stability of photocatalyst in electrolyte solution is very significant for its real-life use in PEC applications [49, 68]. The α-Fe_2O_3/CuO photoanode achieved enhanced light harvesting and photocurrent density, however, its poor stability in electrolyte will inhibit its practical application in photocatalytic hydrogen production. Previously, the stability of CuO-based photoelectrodes has been greatly improved through the deposition of a thin layer of activated carbon [69], metal nanoparticles such as platinum [67] and thin protective layer of TiO_2 [70] on the surface of the films to limit photocorrosion in CuO. Future work on α-Fe_2O_3/CuO should priorities the enhancement of its stability in electrolyte by exploiting one or more of the possible routes of limiting photocorrosion in CuO.

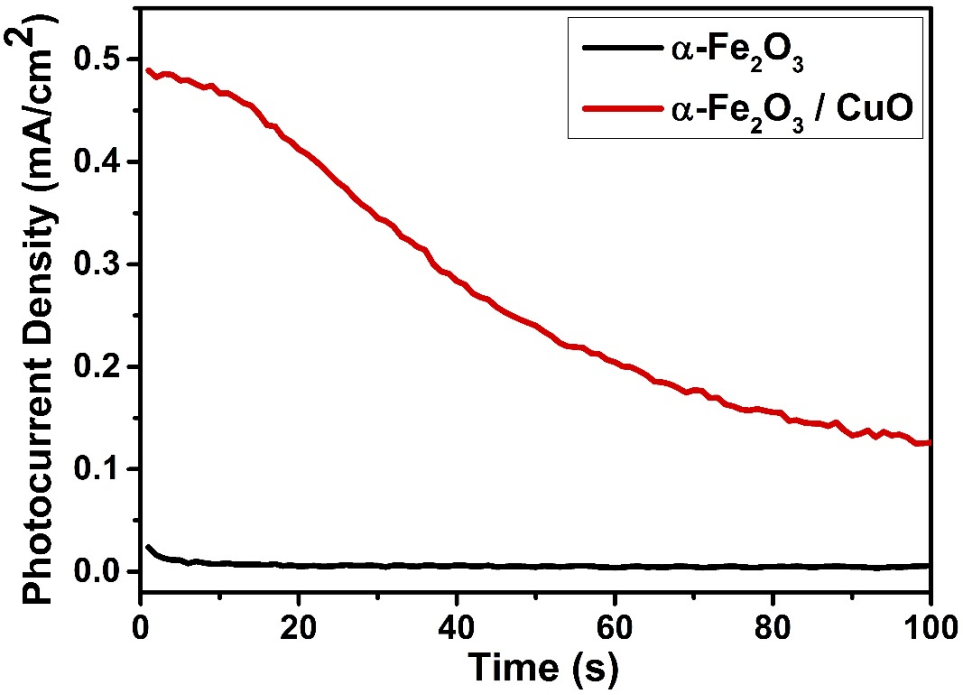

Fig. 11. The stability measurements of α-Fe_2O_3 and α-Fe_2O_3/CuO films.

4 Conclusion

In this research, α-Fe_2O_3/CuO heterojunction photoanode was prepared by dip coating and the impact of the formation of the heterostructure on the PEC properties of α-Fe_2O_3 films was studied. A new approach of preparing porous CuO developed in this project was used in formation of the heterostructure with α-Fe_2O_3. XRD and Raman spectroscopy studies confirmed high purity of α-Fe_2O_3/CuO heterostructures produced. The photocurrent density of 0.53 mA/cm^2 at 1 V vs. RHE was recorded for α-Fe_2O_3/CuO denoting a 19-fold increment when compared to the value obtained for pristine α-Fe_2O_3 films. The formation of a heterojunction structure produced an in-built electric field that facilitated the movement of photoexcited charge carriers which significantly reduced recombination of electron-hole pairs and impacted positively on PEC water splitting. The reduced band gap of α-Fe_2O_3/CuO heterostructure enhanced absorption of photons in the visible region which influenced the improvement in the photocurrent density achieved. The porous surface morphology observed for α-Fe_2O_3/CuO can lead to improved charge separation of photogenerated electron-hole pairs and helped in enhancing PEC water splitting. Furthermore, increase in charge carrier density and the lowering of charge transfer resistance at the photoelectrode/electrolyte interface recorded for α-Fe_2O_3/CuO photoanodes were additional evidence associated with the improvement in photocurrent density for the films. This study presents the formation of α-Fe_2O_3/CuO heterojunction structure with porous surface as a viable route for achieving notable enhancement in the photo response of hematite photoanodes in PEC water splitting.

Acknowledgements

We gratefully acknowledge funding from the National Research Foundation and the World Academy of Sciences (NRF-TWAS), grant UID; 110814, South African Research Chairs Initiative (SARCHI), UID; 115463 and the University of Pretoria. We also acknowledge

financial support from the CSIR National Laser Centre Rental Pool Programme, NRF N00500, UID; 112085 (NRF Research Development Grant) and project UID; 110983 (Blue Skies Research Programme) towards the purchase of a VersaStat 3F potentiostat utilized in this research.

References

[1] Z. Liu, L. Yan, High-efficiency p–n junction oxide photoelectrodes for photoelectrochemical water splitting, Physical Chemistry Chemical Physics, 18 (2016) 31230-31237.

[2] S. Goyal, M.S. Shaharun, C.F. Kait, B. Abdullah, M. Ameen, Photoreduction of Carbon Dioxide to Methanol over Copper Based Zeolitic Imidazolate Framework-8: A New Generation Photocatalyst, Catalysts, 8 (2018) 581.

[3] A. Fujishima, K. Honda, Electrochemical photolysis of water at a semiconductor electrode, nature, 238 (1972) 37.

[4] J. Sun, L. Sun, X. Yang, S. Bai, R. Luo, D. Li, A. Chen, Photoanode of coupling semiconductor heterojunction and catalyst for solar PEC water splitting, Electrochimica Acta, 331 (2020) 135282.

[5] G. Ren, Y. Sun, M. Sun, Y. Li, A. Lu, H. Ding, Visible light enhanced extracellular electron transfer between a hematite photoanode and Pseudomonas aeruginosa, Minerals, 7 (2017) 230.

[6] P. Dias, A. Vilanova, T. Lopes, L. Andrade, A. Mendes, Extremely stable bare hematite photoanode for solar water splitting, Nano Energy, 23 (2016) 70-79.

[7] M.H. Lee, J.H. Park, H.S. Han, H.J. Song, I.S. Cho, J.H. Noh, K.S. Hong, Nanostructured Ti-doped hematite (α-Fe2O3) photoanodes for efficient photoelectrochemical water oxidation, International journal of hydrogen energy, 39 (2014) 17501-17507.

[8] L. Xi, K.M. Lange, Surface modification of hematite photoanodes for improvement of photoelectrochemical performance, Catalysts, 8 (2018) 497.

[9] A. Annamalai, P.S. Shinde, T.H. Jeon, H.H. Lee, H.G. Kim, W. Choi, J.S. Jang, Fabrication of superior α-Fe2O3 nanorod photoanodes through ex-situ Sn-doping for solar water splitting, Solar Energy Materials and Solar Cells, 144 (2016) 247-255.

[10] S.K. Sarma, R. Mohan, A. Shukla, Structural, opto-electronic and photoelectrochemical properties of tin doped hematite nanoparticles for water splitting, Materials Science in Semiconductor Processing, 108 (2020) 104873.

[11] N.M. Ito, W.M. Carvalho, D.N.F. Muche, R.H.R. Castro, G.M. Dalpian, F.L. Souza, High temperature activation of hematite nanorods for sunlight driven water oxidation reaction, Physical Chemistry Chemical Physics, 19 (2017) 25025-25032.

[12] D.H. Kim, D.M. Andoshe, Y.-S. Shim, C.-W. Moon, W. Sohn, S. Choi, T.L. Kim, M. Lee, H. Park, K. Hong, Toward high-performance hematite nanotube photoanodes:

charge-transfer engineering at heterointerfaces, ACS applied materials & interfaces, 8 (2016) 23793-23800.

[13] E.L. Tsege, T.S. Atabaev, M.A. Hossain, D. Lee, H.-K. Kim, Y.-H. Hwang, Cu-doped flower-like hematite nanostructures for efficient water splitting applications, Journal of Physics and Chemistry of Solids, 98 (2016) 283-289.

[14] S.Y. Chiam, M.H. Kumar, P.S. Bassi, H.L. Seng, J. Barber, L.H. Wong, Improving the efficiency of hematite nanorods for photoelectrochemical water splitting by doping with manganese, ACS applied materials & interfaces, 6 (2014) 5852-5859.

[15] H. Bemana, S. Rashid-Nadimi, Effect of sulfur doping on photoelectrochemical performance of hematite, Electrochimica Acta, 229 (2017) 396-403.

[16] H. Bemana, S. Rashid-Nadimi, Incorporation of NiO electrocatalyst with α-Fe2O3 photocatalyst for enhanced and stable photoelectrochemical water splitting, Surfaces and Interfaces, 14 (2019) 184-191.

[17] R. van de Krol, Y. Liang, An n-Si/n-Fe2O3 heterojunction tandem photoanode for solar water splitting, CHIMIA International Journal for Chemistry, 67 (2013) 168-171.

[18] P.S. Bassi, L. Xianglin, Y. Fang, J.S.C. Loo, J. Barber, L.H. Wong, Understanding charge transport in non-doped pristine and surface passivated hematite (Fe 2 O 3) nanorods under front and backside illumination in the context of light induced water splitting, Physical Chemistry Chemical Physics, 18 (2016) 30370-30378.

[19] D. Sharma, S. Upadhyay, A. Verma, V.R. Satsangi, R. Shrivastav, S. Dass, Nanostructured Ti-Fe2O3/Cu2O heterojunction photoelectrode for efficient hydrogen production, Thin Solid Films, 574 (2015) 125-131.

[20] S.J. Moniz, S.A. Shevlin, D.J. Martin, Z.-X. Guo, J. Tang, Visible-light driven heterojunction photocatalysts for water splitting–a critical review, Energy & Environmental Science, 8 (2015) 731-759.

[21] J. Li, F. Meng, S. Suri, W. Ding, F. Huang, N. Wu, Photoelectrochemical performance enhanced by a nickel oxide–hematite p–n junction photoanode, Chemical communications, 48 (2012) 8213-8215.

[22] M.G. Ahmed, T.A. Kandiel, A.Y. Ahmed, I. Kretschmer, F. Rashwan, D. Bahnemann, Enhanced photoelectrochemical water oxidation on nanostructured hematite photoanodes via p-CaFe2O4/n-Fe2O3 heterojunction formation, The Journal of Physical Chemistry C, 119 (2015) 5864-5871.

[23] E.C. Pastrana, V. Zamora, D. Wang, H. Alarcón, Fabrication and characterization of α-Fe2O3/CuO heterostructure thin films via dip-coating technique for improved photoelectrochemical performance, Advances in Natural Sciences: Nanoscience and Nanotechnology, 10 (2019) 035012.

[24] A.G. Tamirat, J. Rick, A.A. Dubale, W.-N. Su, B.-J. Hwang, Using hematite for photoelectrochemical water splitting: a review of current progress and challenges, Nanoscale Horizons, 1 (2016) 243-267.

[25] P.I. Kyesmen, N. Nombona, M. Diale, Influence of coating techniques on the optical and structural properties of hematite thin films, Surfaces and Interfaces, 17 (2019) 100384.

[26] D.H. Taffa, I. Hamm, C. Dunkel, I. Sinev, D. Bahnemann, M. Wark, Electrochemical deposition of Fe 2 O 3 in the presence of organic additives: a route to enhanced photoactivity, RSC Advances, 5 (2015) 103512-103522.

[27] A.G. Tamirat, A.A. Dubale, W.-N. Su, H.-M. Chen, B.-J. Hwang, Sequentially surface modified hematite enables lower applied bias photoelectrochemical water splitting, Physical Chemistry Chemical Physics, 19 (2017) 20881-20890.

[28] S. Krehula, M. Ristić, Ž. Petrović, L.K. Krehula, I. Mitar, S. Musić, Effects of Cu doping on the microstructural, thermal, optical and photocatalytic properties of α-FeOOH and α-Fe2O3 1D nanoparticles, Journal of Alloys and Compounds, 802 (2019) 290-300.

[29] E.J. de Melo, J.P. de Mesquita, M.C. Pereira, L.C.D. Cavalcante, E. dos Santos Filho, J.D. Fabris, J.D. Ardisson, L.C.A. de Oliveira, Synthesis and characterization of αFe 2− x M x O 3 (M= Co, Ni, Cu or Zn) photocatalysts for the degradation of the indigo carmine dye in water, Hyperfine Interactions, 238 (2017) 59.

[30] H. Liu, T. Peng, H. Sun, R. Xie, G. Ma, Room temperature methane sensing properties of α-Fe 2− x Cu x O 3 nanoparticles, RSC Advances, 7 (2017) 11414-11419.

[31] S.S. Ramya, C. Mahadevan, Preparation and structural, optical, magnetic, and electrical characterization of Mn2+/Co2+/Cu2+ doped hematite nanocrystals, Journal of Solid State Chemistry, 211 (2014) 37-50.

[32] T.H. Tran, V.T. Nguyen, Copper oxide nanomaterials prepared by solution methods, some properties, and potential applications: a brief review, International scholarly research notices, 2014 (2014).

[33] A.M. Jubb, H.C. Allen, Vibrational spectroscopic characterization of hematite, maghemite, and magnetite thin films produced by vapor deposition, ACS Applied Materials & Interfaces, 2 (2010) 2804-2812.

[34] B.J. Rani, G. Ravi, R. Yuvakkumar, S. Ravichandran, F. Ameen, S. AlNadhary, Sn doped α-Fe2O3 (Sn= 0, 10, 20, 30 wt%) photoanodes for photoelectrochemical water splitting applications, Renewable Energy, 133 (2019) 566-574.

[35] D. Wang, S. Gao, C. Li, Y. Wang, H. Zhu, Y. Liu, X. Zhang, Pulse laser annealing activates titanium-doped hematite photoanodes for photoelectrochemical water oxidation, Applied Surface Science, 528 (2020) 147062.

[36] D.N. Waters, Raman spectroscopy of powders: effects of light absorption and scattering, Spectrochimica Acta Part A: Molecular Spectroscopy, 50 (1994) 1833-1840.

[37] H. Wang, C.K. Mann, T.J. Vickers, Effect of powder properties on the intensity of Raman scattering by crystalline solids, Applied spectroscopy, 56 (2002) 1538-1544.

[38] S. Shen, J. Jiang, P. Guo, L. Guo, Facile growth of porous hematite films for photoelectrochemical water splitting, International Journal of Photoenergy, 2013 (2013).

[39] K. Sivula, F. Le Formal, M. Grätzel, Solar water splitting: progress using hematite (α-Fe2O3) photoelectrodes, ChemSusChem, 4 (2011) 432-449.

[40] Y. Li, Z. Liu, Y. Wang, Z. Liu, J. Han, J. Ya, ZnO/CuInS2 core/shell heterojunction nanoarray for photoelectrochemical water splitting, international journal of hydrogen energy, 37 (2012) 15029-15037.

[41] N. Subha, M. Mahalakshmi, M. Myilsamy, B. Neppolian, V. Murugesan, Direct Z-scheme heterojunction nanocomposite for the enhanced solar H2 production, Applied Catalysis A: General, 553 (2018) 43-51.

[42] Y. Zhao, Y. Lin, G. Wang, Z. Jiang, R. Zhang, C. Zhu, Photocatalytic water splitting of (F, Ti) codoped heptazine/triazine based g-C3N4 heterostructure: A hybrid DFT study, Applied Surface Science, 463 (2019) 809-819.

[43] S. Xiao, C. Hu, H. Lin, X. Meng, Y. Bai, T. Zhang, Y. Yang, Y. Qu, K. Yan, J. Xu, Integration of inverse nanocone array based bismuth vanadate photoanodes and bandgap-tunable perovskite solar cells for efficient self-powered solar water splitting, Journal of Materials Chemistry A, 5 (2017) 19091-19097.

[44] A.K. Singh, D. Sarkar, A facile approach for preparing densely-packed individual p-NiO/n-Fe 2 O 3 heterojunction nanowires for photoelectrochemical water splitting, Nanoscale, 10 (2018) 13130-13139.

[45] S. Bai, J. Liu, M. Cui, R. Luo, J. He, A. Chen, Two-step electrodeposition to fabricate the p–n heterojunction of a Cu 2 O/BiVO 4 photoanode for the enhancement of photoelectrochemical water splitting, Dalton Transactions, 47 (2018) 6763-6771.

[46] A. Kargar, K. Sun, Y. Jing, C. Choi, H. Jeong, G.Y. Jung, S. Jin, D. Wang, 3D Branched nanowire photoelectrochemical electrodes for efficient solar water splitting, ACS nano, 7 (2013) 9407-9415.

[47] K. Sun, Y. Jing, C. Li, X. Zhang, R. Aguinaldo, A. Kargar, K. Madsen, K. Banu, Y. Zhou, Y. Bando, 3D branched nanowire heterojunction photoelectrodes for high-efficiency solar water splitting and H 2 generation, Nanoscale, 4 (2012) 1515-1521.

[48] J. Hou, C. Yang, H. Cheng, S. Jiao, O. Takeda, H. Zhu, High-performance p-Cu 2 O/n-TaON heterojunction nanorod photoanodes passivated with an ultrathin carbon sheath for photoelectrochemical water splitting, Energy & Environmental Science, 7 (2014) 3758-3768.

[49] K. Afroz, M. Moniruddin, N. Bakranov, S. Kudaibergenov, N. Nuraje, A heterojunction strategy to improve the visible light sensitive water splitting performance of photocatalytic materials, Journal of Materials Chemistry A, 6 (2018) 21696-21718.

[50] N. Dasineh Khiavi, R. Katal, S. Kholghi Eshkalak, S. Masudy-Panah, S. Ramakrishna, H. Jiangyong, Visible Light Driven Heterojunction Photocatalyst of CuO–Cu2O Thin Films for Photocatalytic Degradation of Organic Pollutants, Nanomaterials, 9 (2019) 1011.

[51] T. Lopes, L. Andrade, F. Le Formal, M. Gratzel, K. Sivula, A. Mendes, Hematite photoelectrodes for water splitting: evaluation of the role of film thickness by impedance spectroscopy, Physical Chemistry Chemical Physics, 16 (2014) 16515-16523.

[52] Y. Wei, A. Liao, L. Wang, X. Wang, D. Wang, Y. Zhou, Z. Zou, Room Temperature Surface Modification of Ultrathin FeOOH Cocatalysts on Fe2O3 Photoanodes for High Photoelectrochemical Water Splitting, Journal of Nanomaterials, 2020 (2020).

[53] L. Hamadou, L. Aïnouche, A. Kadri, S.A.A. Yahia, N. Benbrahim, Electrochemical impedance spectroscopy study of thermally grown oxides exhibiting constant phase element behaviour, Electrochimica Acta, 113 (2013) 99-108.

[54] C. Han, L. Yan, W. Zhao, Z. Liu, TiO2/CeO2 core/shell heterojunction nanoarrays for highly efficient photoelectrochemical water splitting, International Journal of Hydrogen Energy, 42 (2017) 12276-12283.

[55] C. Hao, W. Wang, R. Zhang, B. Zou, H. Shi, Enhanced photoelectrochemical water splitting with TiO2@ Ag2O nanowire arrays via pn heterojunction formation, Solar Energy Materials and Solar Cells, 174 (2018) 132-139.

[56] S. Cao, X. Yan, Z. Kang, Q. Liang, X. Liao, Y. Zhang, Band alignment engineering for improved performance and stability of ZnFe2O4 modified CdS/ZnO nanostructured photoanode for PEC water splitting, Nano Energy, 24 (2016) 25-31.

[57] C. Niveditha, M.J. Fatima, S. Sindhu, Comprehensive interfacial study of potentio-dynamically synthesized copper oxide thin films for photoelectrochemical applications, Journal of The Electrochemical Society, 163 (2016) H426-H433.

[58] F. Zhan, Y. Yang, W. Li, J. Li, W. Liu, Y. Li, Q. Chen, Preparation of DyVO 4/WO 3 heterojunction plate array films with enhanced photoelectrochemical activity, RSC advances, 6 (2016) 10393-10400.

[59] Z. Zhang, P. Wang, Optimization of photoelectrochemical water splitting performance on hierarchical TiO 2 nanotube arrays, Energy & Environmental Science, 5 (2012) 6506-6512.

[60] M. Alizadeh, G.B. Tong, M.S. Mehmood, K.W. Qader, S.A. Rahman, B. Shokri, Band engineered Al-rich InAlN thin films as a promising photoanode for hydrogen generation from solar water splitting, Solar Energy Materials and Solar Cells, 185 (2018) 445-455.

[61] Z. Zhang, P. Wang, Highly stable copper oxide composite as an effective photocathode for water splitting via a facile electrochemical synthesis strategy, Journal of Materials Chemistry, 22 (2012) 2456-2464.

[62] Y. Liang, C.S. Enache, R. van de Krol, Photoelectrochemical Characterization of Sprayed, International Journal of Photoenergy, 2008 (2008).

[63] E. Aguilera-Ruiz, M. De La Garza-Galván, P. Zambrano-Robledo, J. Ballesteros-Pacheco, J. Vazquez-Arenas, J. Peral, U. García-Pérez, Facile synthesis of visible-light-driven Cu 2 O/BiVO 4 composites for the photomineralization of recalcitrant pesticides, RSC advances, 7 (2017) 45885-45895.

[64] P. Liao, E.A. Carter, Hole transport in pure and doped hematite, Journal of Applied Physics, 112 (2012) 013701.

[65] Y. Zhang, W. Li, Z. Sun, Q. Zhang, L. Wang, Z. Chen, In-situ synthesis of heterostructured BiVO4/BiOBr core-shell hierarchical mesoporous spindles with highly enhanced visible-light photocatalytic performance, Journal of Alloys and Compounds, 713 (2017) 78-86.

[66] J.Y. Kim, J.W. Jang, D.H. Youn, G. Magesh, J.S. Lee, A stable and efficient hematite photoanode in a neutral electrolyte for solar water splitting: towards stability engineering, Advanced Energy Materials, 4 (2014) 1400476.

[67] H. Xing, E. Lei, Z. Guo, D. Zhao, X. Li, Z. Liu, Exposing the photocorrosion mechanism and control strategies of a CuO photocathode, Inorganic Chemistry Frontiers, 6 (2019) 2488-2499.

[68] W.Z. Tawfik, M.A. Hassan, M.A. Johar, S.-W. Ryu, J.K. Lee, Highly conversion efficiency of solar water splitting over p-Cu2O/ZnO photocatalyst grown on a metallic substrate, Journal of Catalysis, 374 (2019) 276-283.

[69] P.P. Kunturu, J. Huskens, Efficient Solar Water Splitting Photocathodes Comprising a Copper Oxide Heterostructure Protected by a Thin Carbon Layer, ACS Applied Energy Materials, 2 (2019) 7850-7860.

[70] J. Toupin, H. Strubb, S. Kressman, V. Artero, N. Krins, C. Laberty-Robert, CuO photoelectrodes synthesized by the sol–gel method for water splitting, Journal of Sol-Gel Science and Technology, 89 (2019) 255-263.